Downloaded from orbit.dtu.dk on: Apr 30, 2024

DTU Library

Computational engineering of the oxygen electrode-electrolyte interface in solid oxide fuel cells

Cheng, Kaiming; Xu, Huixia; Zhang, Lijun; Zhou, Jixue; Wang, Xitao; Du, Yong; Chen, Ming

Published in:
npj Computational Materials

Link to article, DOI:
10.1038/s41524-021-00584-8

Publication date:
2021

Document Version
Publisher's PDF, also known as Version of record

Link back to DTU Orbit

Citation (APA):
Cheng, K., Xu, H., Zhang, L., Zhou, J., Wang, X., Du, Y., & Chen, M. (2021). Computational engineering of the oxygen electrode-electrolyte interface in solid oxide fuel cells. *npj Computational Materials*, *7*(1), Article 119. https://doi.org/10.1038/s41524-021-00584-8

General rights
Copyright and moral rights for the publications made accessible in the public portal are retained by the authors and/or other copyright owners and it is a condition of accessing publications that users recognise and abide by the legal requirements associated with these rights.

- Users may download and print one copy of any publication from the public portal for the purpose of private study or research.
- You may not further distribute the material or use it for any profit-making activity or commercial gain
- You may freely distribute the URL identifying the publication in the public portal

If you believe that this document breaches copyright please contact us providing details, and we will remove access to the work immediately and investigate your claim.

npj Computational Materials

www.nature.com/npjcompumats

ARTICLE OPEN

Computational engineering of the oxygen electrode-electrolyte interface in solid oxide fuel cells

Kaiming Cheng[1,2], Huixia Xu[2,3,4], Lijun Zhang[4], Jixue Zhou[1]✉, Xitao Wang[1], Yong Du[1,4] and Ming Chen[2]✉

The $Ce_{0.8}Gd_{0.2}O_{2-\delta}$ (CGO) interlayer is commonly applied in solid oxide fuel cells (SOFCs) to prevent chemical reactions between the $(La_{1-x}Sr_x)(Co_{1-y}Fe_y)O_{3-\delta}$ (LSCF) oxygen electrode and the Y_2O_3-stabilized ZrO_2 (YSZ) electrolyte. However, formation of the YSZ–CGO solid solution with low ionic conductivity and the $SrZrO_3$ (SZO) insulating phase still happens during cell production and long-term operation, causing poor performance and degradation. Unlike many experimental investigations exploring these phenomena, consistent and quantitative computational modeling of the microstructure evolution at the oxygen electrode–electrolyte interface is scarce. We combine thermodynamic, 1D kinetic, and 3D phase-field modeling to computationally reproduce the element redistribution, microstructure evolution, and corresponding ohmic loss of this interface. The influences of different ceramic processing techniques for the CGO interlayer, i.e., screen printing and physical laser deposition (PLD), and of different processing and long-term operating parameters are explored, representing a successful case of quantitative computational engineering of the oxygen electrode–electrolyte interface in SOFCs.

npj Computational Materials (2021)7:119; https://doi.org/10.1038/s41524-021-00584-8

INTRODUCTION

Owing to the advantages of high-energy efficiency, broad fuel options, low pollutant emissions, and scalable stacks, solid oxide fuel cells (SOFCs) are attracting increasing attention in the clean and efficient generation of electrical power from renewable sources. However, worldwide commercialization of SOFCs is hindered due to problems induced by the high operating temperature, i.e., high material cost and materials degradation during long-term operation. Within the past two decades, significant progress has been made in the selection of suitable materials of SOFCs to reduce operating temperature from ~1000 to 500–800 °C, of which the latter is known as the intermediate temperature SOFCs (IT-SOFCs)[1,2].

Generally speaking, the structure of an SOFC cell consists of a dense electrolyte sandwiched by two porous electrodes (cathode and anode). The electrolyte transports oxygen ions from the cathode, where the oxygen is being reduced into oxygen ions, to the anode. High ionic conductivity is an important prerequisite when selecting the electrolyte materials. 8 mol.% yttria-stabilized zirconia (8YSZ) is the most wildly used electrolyte material so far. Within the intermediate temperature range, gadolinia-doped ceria (CGO) with high ionic conductivity is also regarded as a good electrolyte material for IT-SOFCs, though it may exhibit a minor degree of electronic conductivity at temperatures above 550 °C, reducing the SOFC efficiency[3]. The cathode is devoted to reducing oxygen molecules into O^{2-} ions. For IT-SOFCs, the $(La_{1-x}Sr_x)(Co_{1-y}Fe_y)O_{3-\delta}$ (LSCF) perovskite with mixed ionic and electronic conductivity (MIEC), good catalytic properties, and good stability has been widely adopted as the cathode material[4,5]. Unfortunately, LSCF reacts with YSZ, forming insulating phases of $La_2Zr_2O_7$ and $SrZrO_3$[6]. A reaction barrier layer made from CGO is often required. The anode material should possess high electronic conductivity and good electrocatalytic activity for fuel oxidation and electrons release. The most commonly used anode material for IT-SOFCs is Ni-YSZ cermet since its invention in 1970, and this situation seems to remain until considerable improvement is reached in the future development of oxide-based anode materials[2]. In addition to the outstanding performance of the individual materials mentioned above, good mechanical stability and chemical inertness between each component of IT-SOFCs are stringent requirements to develop high-performing and durable full cells[7]. Considering these, the anode-supported Ni-YSZ (anode)/YSZ (electrolyte)/CGO (barrier)/LSCF (cathode) cells are the state of art IT-SOFCs having promising initial performance in the desired temperature range[5,8].

The LSCF cathode suffers from performance degradation, which to a large extent is caused by phase transformation or microstructural changes. Apart from the degradation processes in LSCF itself, such as Cr poisoning, sulfur poisoning, coarsening of the microstructure, and loss of conductivity etc.[8–12], interactions of the YSZ electrolyte with the CGO barrier as well as the LSCF cathode are two important contributors to the degradation[13–16]. In an IT-SOFC with the LSCF cathode, the CGO barrier layer is introduced to limit the interdiffusion and reaction between the LSCF cathode and the YSZ electrolyte, which otherwise will lead to formation of insulating phases, e.g., $La_2Zr_2O_7$ (LZO) and $SrZrO_3$ (SZO). CGO is chosen as the material for the barrier layer, not only due to its high ionic conductivity at intermediate temperature range as mentioned above but also due to its good chemical and thermomechanical compatibility with YSZ and LSCF[13,17–20]. The literature reported CGO barrier layer is effective, but not yet sufficient to completely stop the interdiffusion and formation of zirconate phases. The above degradation phenomena still happen in IT-SOFCs with LSCF cathode during either cell fabrication or long-term operation as described further below.

In order to fabricate the YSZ (dense)/CGO (preferably dense)/LSCF (porous) structure, wet deposition techniques, e.g., screen

[1]Shandong Provincial Key Laboratory of High Strength Lightweight Metallic Materials, Advanced Materials Institute, Qilu University of Technology (Shandong Academy of Sciences), Jinan, China. [2]Department of Energy Conversion and Storage, Technical University of Denmark, Lyngby Campus, Kgs, Lyngby, Denmark. [3]Engineering Research Center of Failure Analysis and Safety Assessment, Shandong Analysis and Test Center, Qilu University of Technology (Shandong Academy of Sciences), Jinan, China. [4]State Key Laboratory of Powder Metallurgy, Central South University, Changsha, China. ✉email: zhoujx@sdas.org; minc@dtu.dk

Published in partnership with the Shanghai Institute of Ceramics of the Chinese Academy of Sciences

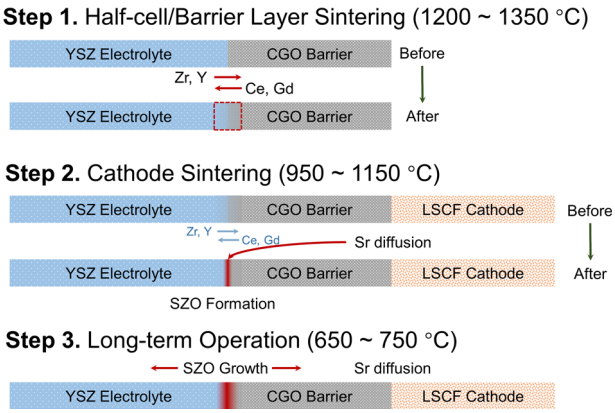

Fig. 1 Schematic diagram of the oxygen electrode–electrolyte interface reactions. The interdiffusion and reaction processes happening in the YSZ–CGO–LSCF region during cell fabrication (Steps 1 and 2) and long-term operation (Step 3) of IT-SOFCs with LSCF cathode.

printing, spray deposition, and dip coating, are commonly employed. Usually, a two-step sintering is performed, during which the interdiffusion and reactions already take place, as illustrated in Fig. 1. In this work, the fuel electrode side is not taken into consideration. On the oxygen electrode side, we divide the relevant cell production and operation into three steps. In Step 1, a CGO layer is deposited on the pre-sintered YSZ electrolyte followed by high-temperatures sintering (1200–1350 °C) to achieve an effectively dense diffusion barrier layer of CGO. Such high temperatures can activate the interdiffusion processes between CGO and YSZ, which eventually leads to the formation of a $CGO_xYSZ_{(1-x)}$ solid solution with low ionic conductivity, the well-known Kirkendall voids, or even dopant migration[13,14,17,20–22]. In Step 2, a LSCF layer is deposited on the CGO layer, followed by sintering at a slightly lower temperature (950–1150 °C), where the interdiffusion across the YSZ–CGO interface will still continue, but in a much less degree due to much slower diffusion kinetics. Despite of the existence of the CGO barrier layer, formation of the SZO phase at the YSZ–CGO interface is confirmed by a large number of experimental investigations so far[13,15,22–30]. Sr accumulated at the YSZ–CGO interface is believed to diffuse from the LSCF cathode through the CGO barrier layer mainly during the cathode-sintering process. During the long-term operation process, i.e., Step 3 in Fig. 1, the kinetics of Sr diffusion (at 650–750 °C) is much slower than in Step 2. But the growth of SZO at the YSZ–CGO interface continues and contributes to the cell long-term degradation when the operation time reaches a magnitude of $>10^3$ h[16,24,28]. A dense CGO barrier layer realized without high-temperature sintering can effectively limit these interdiffusion-induced degradation processes. Pulsed laser deposition (PLD), or physical vapor deposition (PVD), is applicable to produce thin and dense CGO epitaxy on YSZ substrate[16,22,23]. Other methods, such as co-firing of the YSZ and CGO layers at reduced temperature utilizing a sintering aid, provides the possibility of compositional and microstructural engineering[31]. Nevertheless, screen printing is so far the most widely adopted method for producing the CGO barrier layer (and the LSCF cathode as well), considering its high deposition rate and low cost, though it is difficult to achieve a fully dense CGO barrier layer as by PLD or PVD.

The area-specific resistance (ASR) is a common variable to represent the performance of SOFC cells. The ASR can be split into polarization and ohmic resistance. The ohmic resistance (ASR_Ω) can be ascribed to mainly the electrolyte resistance[32]. The interdiffusion between YSZ and CGO and the formation of the $CGO_xYSZ_{(1-x)}$ solid solution causes a significant increase in the ohmic resistance. Recent studies indicate that this part of performance degradation depends strongly on the fabrication method of the CGO barrier layer (e.g., screen printing or PLD, etc.) as well as the fabrication conditions (e.g., sintering temperature and time)[16,28,29]. The PLD method avoids the barrier layer sintering step (Step 1) where most of the YSZ–CGO interdiffusion takes place. In addition, it can produce a thin dense CGO layer with a large grain size to slow down the Sr diffusion, resulting in a very little increment in ASR_Ω after cathode sintering (Step 2) and after the long-term operation (Step 3)[16]. For a screen-printed CGO barrier layer, achieving high densification often requires a high sintering temperature (>1200 °C) in Step 1. This results in significant YSZ–CGO interdiffusion and thus increment of ASR_Ω. The resulting YSZ–CGO interdiffusion zone can further influence the Sr diffusion and formation of SZO in Steps 2 and 3[29]. The higher the CGO sintering temperature, the denser the CGO layer, the more the CGO–YSZ interdiffusion, however the less the Sr diffusion and SZO formation. This makes it difficult to identify appropriate fabrication parameters in order to reach an optimum condition to minimize both the YSZ–CGO interdiffusion and the SZO formation. Moreover, it is even harder to derive a general rule by making a crosswise comparison among the experimental results existing in the literature, since the fabrication conditions of the tested cells from different labs are hardly the same. Considering the above, computational numerical modeling of the microstructure evolution in SOFCs shall be performed not only to reproduce the kinetic and microstructural changes observed experimentally but also to correlate with the cell performance, hence be able to provide a reliable prediction of cell performance as functions of fabrication and long-term operation conditions. If successful, this will open a new route of computational engineering of the oxygen electrode–electrolyte interface, targeting both superior initial performance and good long-term durability.

Recently, the current authors have tried modeling the YSZ–CGO interdiffusion and thin layer SZO formation at the YSZ–CGO interface[33,34]. Several simplifications were made in the model, e.g., consideration of no CGO grain growth during high-temperature sintering and treating the SZO phase as a continuous layer instead of dispersed distribution. These simplifications do not reflect what actually happens in IT-SOFCs. To the best of our knowledge, no other computational study has been reported which models the CGO–YSZ interdiffusion, Sr diffusion, and SZO formation during cell production and long-term operation in a systematic way. This is thus the aim of the current work: (i) to develop a set of thermodynamic and diffusion kinetic databases providing an accurate description of the phase relations and elemental diffusivities in the YSZ–CGO–LSCF system based on the calculation of the phase diagram (CALPHAD) approach; (ii) to kinetically model the experimentally observed[16,24,28] YSZ–CGO interdiffusion, Sr diffusion across the CGO layer and formation of SZO by performing both one dimension (1D) solid-state reaction and three-dimension (3D) phase-field simulations; (iii) to identify the correlations between the cell fabrication and operation parameters, the microstructures, and the ohmic resistance according to the current simulation results, and compare with the previous experimental findings[29].

RESULTS AND DISCUSSION

Simulation of SZO formation in screen-printed CGO

Figure 2 plots the simulated composition profiles in comparison with previous experimental data measured at the CGO–YSZ interface ranging from 5 to 11 μm[24], for the case of a SOFC with screen-printed CGO barrier layer during the different steps in cell production and long-term operation. In Fig. 2a, the distribution of Ce and Zr after the barrier layer sintering step at 1523 K for 2 h is presented, showing a ~1-μm thick interdiffusion zone at the interface. We have previously reported a systematic investigation

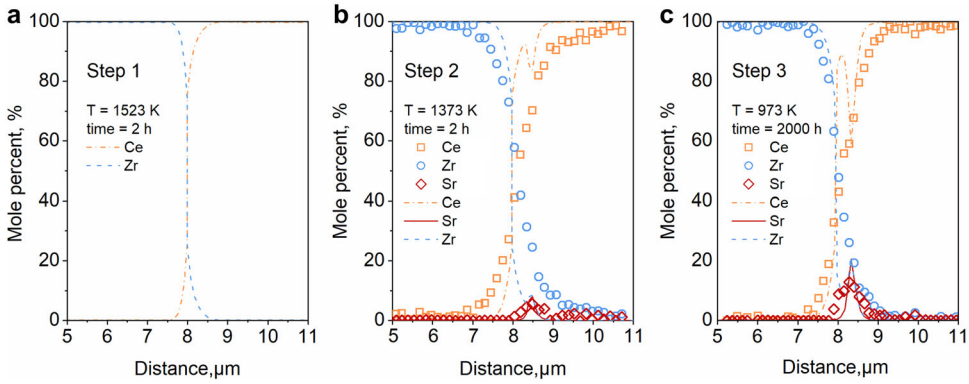

Fig. 2 Composition profiles across the oxygen electrode–electrolyte interface (screen-printed CGO). Simulated composition profiles (dotted lines) in comparison with previous experimental data (scattered symbols)[24], for the case of a SOFC with screen-printed CGO barrier layer during the different steps in (**a**, **b**) cell production and (**c**) long-term operation. The distance at 0 μm corresponds to the left boundary of the ZrO_2 layer, and the original ZrO_2–CeO_2 interface is located at 8 μm.

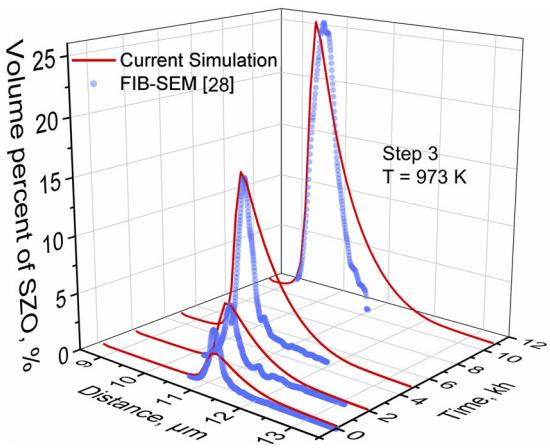

Fig. 3 Simulated and measured SZO formation at the oxygen electrode–electrolyte interface (screen-printed CGO). Amount of formed SZO after different operation time in the case of screen-printed CGO barrier layer predicted from 1D kinetic modeling (red solid lines), compared with the FIB-SEM investigation (blue dotted lines)[28].

on the interdiffusion process between the YSZ electrolyte and the CGO barrier layer, including both experimental investigations and 1D kinetic modeling[33]. The detail will therefore not be repeated here. Figure 2b presents the simulated composition profile after the cathode-sintering step at 1373 K for 2 h compared with the experimental data reported by Kiebach et al.[24]. An accumulation of Sr on the Ce-rich side of the ZrO_2–CeO_2 interface can be clearly observed from the experiment data and is also predicted by the simulation. Why is Sr not accumulated on the ZrO_2-rich side can be well explained by investigating the Sr diffusion route on the isothermal section of the ZrO_2–CeO_2–SrO system. As can be seen from the phase diagram shown in Supplementary Fig. 1, the ZrO_2–SrO binary subsystem represents a direct contact between YSZ and LSCF, where SZO forms due to the reaction between them. When a layer of CeO_2 is placed in between, diffusion of Sr in the Gibbs triangle shall follow the path starting from the SrO corner and going through the SrO–CeO_2 subsystem to reach the ZrO_2–CeO_2 side, as shown in Supplementary Fig. 1. Since there is no intermediate reaction in the SrO–CeO_2 system, Sr will first enter the two-phase region of Cubic + SZO. In order to reach the two-phase equilibrium, Sr diffuses from the right boundary of the CeO_2 layer to the Ce-rich part of the interdiffusion zone (IDZ), and further reacts with the ZrO_2 dissolved in CeO_2 (during the barrier sintering step), and forms SZO in the Ce-rich part of IDZ. As the amount of Sr on the Ce-rich side of IDZ increases, the diffusion front of Sr will finally reach the equilibrium between the miscibility gap of Cubic $ZrO_2 + CeO_2$ and SZO, indicating growth of SZO into the YSZ region. As can be seen in Fig. 2c, when the SOFC cell is tested at 973 K for 2000 h, the diffusion front reaches the original interface between YSZ and CGO. So for the screen-printed CGO barrier layer, the property of CGO and more specifically the IDZ layer which can be controlled by varying the processing conditions, is of great importance with regard to stop or slow down the Sr diffusion and the SZO formation.

Formation of SZO is the result of Sr diffusion across the CGO barrier layer to the Ce-rich side of IDZ and reaction with ZrO_2 dissolved in CeO_2, and the process continues during long-term operation at intermediate temperature (Step 3). Figure 3 shows the simulated amount of formed SZO along the diffusion distance for different operation time at 973 K in the case of screen-printed CGO barrier layer, compared with the systematical investigation by Rinaldi et al.[28]. The numerical modeling was performed considering sintering at 1300 °C for 3 h for the 6-μm thick CGO barrier layer screen-printed on an 8-μm YSZ substrate, followed by screen printing and sintering of the LSCF layer at 1100 °C for 3 h. The long-term operation was performed at 700 °C. The simulated changes in the volume percentage of SZO during the long-term test is recorded at 0, 1900, 4700, and 10,700 h, achieving a reasonable agreement with the experimental data based upon the segmentation of the low kV ESB and InLens grayscale electrons images and complemented with 3D EDX elemental mapping for the 10,700 h sample. It can be seen that the peak value (i.e., the maximum volume percentage of formed SZO) increases from 3% at 0 h (after cell production) to 25% at 10,700 h (after 10,700 h operation at 973 K). The peak position within the IDZ region moves towards the Zr-rich side, which is consistent with the current finding of the Sr diffusion path. A wider distribution of SZO is predicted based on the current simulation, implying a deeper expansion of SZO into the CGO layer. In addition to the simplifications adopted in current modeling, the discard of elastic strain energy could be one reason for the suppression of SZO expansion in the real case. Our simulation result further demonstrates the applicability of current modeling to simulate the formation of SZO in IT-SOFC in the case of the screen-printed CGO barrier layer.

Simulation of the formation of SZO in PLD CGO

Figure 4 plots the simulated SZO formation at the YSZ–CGO interface in the case of PLD CGO, after cathode sintering or during long-term operation. In Fig. 4a, b, formation of SZO is predicted at the CeO_2–ZrO_2 interface, which is of a reasonably small amount in

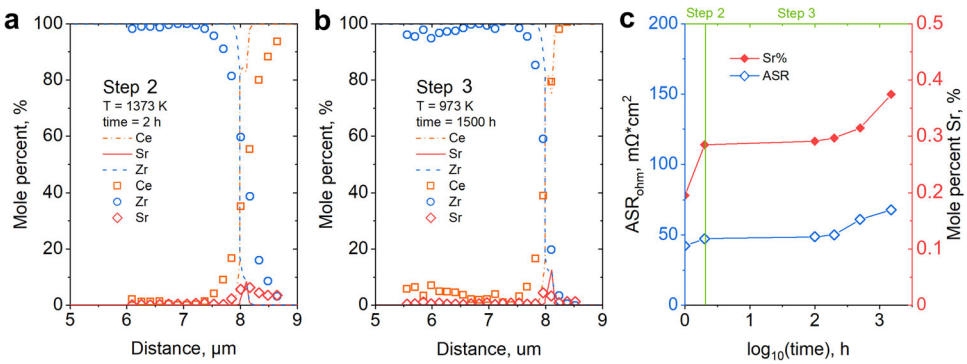

Fig. 4 Composition profiles across the oxygen electrode–electrolyte interface (PLD CGO). a, b Simulation (dashed lines) of the SZO formation at the YSZ–CGO interface during cathode sintering (Step 2) and long-term operation (Step 3) in comparison with the experimental data (scattered symbols)[16]. **c** Estimated amount of Sr in the simulated IDZ and the corresponding ASR_{ohm} at 700 °C. Distance at 0 μm corresponds to the left boundary of the ZrO_2 layer, and the original ZrO_2–CeO_2 interface is located at 8 μm.

agreement with the experimental data measured at the CGO–YSZ interface ranging from 5 to 9 μm. Comparing with the case of the screen-printed CGO barrier layer, i.e., Figure 2, the PLD CGO layer shows a much better effect on hindering the Sr diffusion and the SZO formation. This can also be seen in Fig. 4c that the accumulation of Sr within the simulated IDZ is very slow (<0.3% after 2 h sintering at 1373 K and <0.4% after 1500 h operation at 973 K).

The dense CGO barrier layer deposited by the low-temperature PLD technique eliminates CGO–YSZ intermixing due to no high-temperature sintering, and also prevents extensive SZO formation. Only the grain boundaries in the epitaxial CGO barrier layer facilitate Sr diffusion to the YSZ electrolyte to form SZO[16]. It is also reported that the SZO grain generated at the quadruple junction of the YSZ and epitaxial CGO grains represents an elongated spreading shape along the CGO–YSZ interface[16]. Figure 5 presents the 3D phase-field simulation of the microstructure evolution during SZO formation at 1373 K for 2 h. The simulation results indicate the random formation of SZO at the quadruple junction begins at around 1200 s, during which Sr should diffuse across the CGO barrier layer. The particles merge to form a contiguous region after growth for 1 h, and then grow into an elongated spreading shape along the CGO–YSZ interface due to faster grain boundary diffusion of Sr^{2+}. The distribution of Sr is scanned along two lines of L1 and L2, where the Sr content differences in the bulk and at grain boundaries is ~1.2% and is much lower than that in the regions of SZO and SrO. The simulation result reproduces the experimental findings reported in[16] reasonably well. In Fig. 5, the amount of Sr accumulates within the IDZ is calculated and compared with the result of 1D DICTRA simulation, showing good agreement. These results further prove the current modeling of the SZO formation is also valid in the case of the PLD CGO barrier layer.

Evolution of the ASR_{ohm}

Our current model can also be used to estimate the electrolyte resistance after cell production and during cell long-term operation by using Eq. (9). The previous experimental study[29] demonstrates that the CGO sintering temperature strongly influences the microstructure evolution in the YSZ/CGO/LSZF region. It was shown that the SZO formation is largely reduced by a screen-printed CGO diffusion barrier layer sintered at sufficiently high temperature (1400 °C), forming a dense IDZ at the YSZ–CGO interface, resulting in low ohmic resistance after cathode sintering[29]. The current work tries to simulate these processes as well as to further study the effect of the barrier layer sintering condition. The numerical modeling is chosen to be identical to Fig. 2, and the simulation conditions are selected to keep consistent with the experiment[29], where a 5.5-μm thick screen-printed CGO was sintered at 1100, 1250, and 1400 °C for 3 h on a 200-μm thick YSZ substrate. The subsequently screen-printed LSCF layer (on top of the CGO layer) was sintered at 1100 °C for 3 h, and the cell long-term operation was performed at 800 °C. In this work, DC1, DC2, and DC3 refer to the samples where the CGO layer is sintered at 1100, 1250, and 1400 °C, respectively.

Figure 6 gives the calculated ASR_{ohm} in DC1, DC2, and DC3 at the three stages of barrier layer sintering (Step 1), cathode sintering (Step 2), and long-term operation (Step 3). As for Step 1, compared with the theoretical ASR_{ohm} (433 mΩ cm^2) estimated when no IDZ or SZO forms, DC1 and DC2 show only a slight increase in ASR_{ohm}, i.e., 435 mΩ cm^2 for DC1 with a barrier layer sintering temperature of 1373 K and 438 mΩ cm^2 for DC2 with a barrier layer sintering temperature of 1523 K, indicating weak interdiffusion between YSZ and CGO at lower sintering temperature. The ASR_{ohm} of DC3 sintered at 1673 K reaches 461 mΩ cm^2 after the 3-h barrier layer sintering stage. Figure 7a gives the simulated IDZ thickness for DC1, DC2, and DC3 after the barrier layer sintering at 1100, 1250, and 1400 °C, respectively. It is clear that the IDZ thickness increases with the sintering time, and the growth rate increases with the sintering temperature. Higher temperature for barrier layer sintering leads to faster interdiffusion between CGO and YSZ, and hence results in thicker IDZ and higher ASR_{ohm} after Step 1.

After Step 2, DC1 then exhibits a dramatic increment in ASR_{ohm}: from 430 to 483 mΩ cm^2, which is close to the experimentally measured value of 481 mΩ cm^2 (see ref. [29]). This increment in ASR_{ohm} is mainly due to the formation of SZO at the CGO–YSZ interface. The amount of Sr accumulated in the IDZ is calculated and presented also in Fig. 7. At this stage, it can be seen that DC1 shows the fastest increment of Sr content, while DC2 accumulates slightly more Sr than DC3, implying that DC3 has the best ability to resist SZO formation. This is consistent with the predicted ASR_{ohm} of DC2 (442 mΩ cm^2, increased by 7 mΩ cm^2) and of DC3 (461 mΩ cm^2, nearly unchanged) in Step 2. The current modeling results show a reasonable trend in the case of developing a universal computational model, where all the initial conditions and processing parameters are taken into account. The deviation from the experimentally measured results of DC2 (485 mΩ cm^2) and DC3 (431 mΩ cm^2)[29] can be partly attributed to the simplifications adopted in our model, where no microstructure information (porosity, size, and distribution of SZO, etc.) is taken into account. In addition, the calculation of ASR from Eq. (9), which considers the parallel distribution of cubic solid solution and SZO to calculate the effective resistivity, could be another source of the ASR deviation. Last, but not least, the lack of accurate experimental detail in the published literature (due to

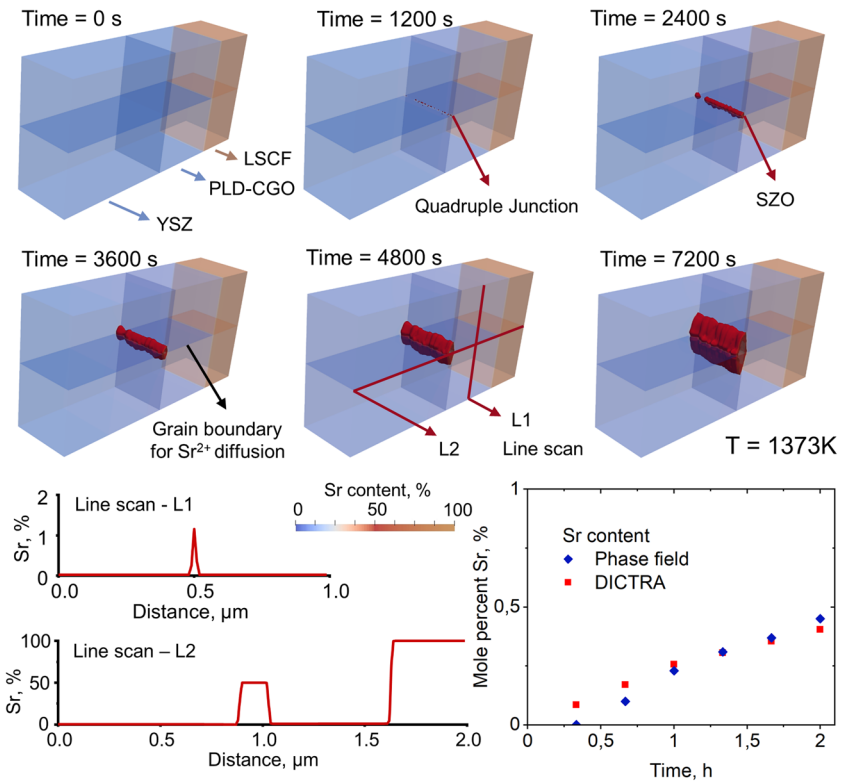

Fig. 5 Phase-field simulation of the oxygen electrode–electrolyte interface reactions (PLD CGO). Simulation of the SZO formation at the YSZ–CGO interface in the case of PLD CGO during cathode sintering at 1373 K for 0, 1200, 2400, 3600, 4800, and 7200 s. The size of 3D phase-field simulation area has been shown in the modeling section. The distribution profiles of Sr are scanned along two lines of L1 and L2, and the amount of Sr accumulates within the IDZ is calculated and compared with the result of 1D DICTRA simulation.

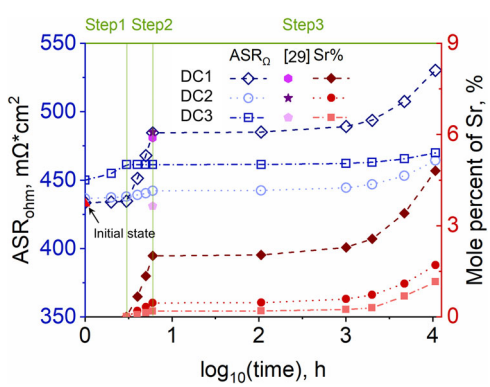

Fig. 6 Predicted ASR_{ohm} change resulting from the oxygen electrode–electrolyte interface reactions. Calculated ASR_{ohm} at 800 °C in DC1, DC2, and DC3 at the three stages of barrier sintering (Step 1), cathode sintering (Step 2), and long-term operation (Step 3) and the amount of Sr accumulated in the IDZ, together with the experimentally measured values[29].

confidentiality and IPR) is another important factor contributing to the deviation from the experimental results.

During long-term operation (Step 3) at 1073 K, DC1 exhibits again the fastest SZO formation. The resulting ASR_{ohm} increases from 483 to 530 mΩ cm^2 after 10,000 h. Apparently, DC1 with CGO barrier layer sintered at 1100 °C shows the worst ability to resist the formation of the SZO phase in both Steps 2 and 3. Although DC2 shows slightly faster Sr accumulation than DC3 at the IDZ, it turns out to show the lowest ASR_{ohm} after 10,000 h (464 mΩ cm^2), since the overall ASR_{ohm} increment in Steps 1 and 2 is the lowest among the three samples. DC3 shows the least Sr diffusion, SZO formation, and thusly the lowest ASR_{ohm} increment from 461 to only 469 mΩ·cm^2 after 10,000 h, indicating the best performance of preventing ohmic loss caused by SZO formation. The major degradation procedure of DC3 should be the very thick IDZ generated in Step 1.

For all the three samples of DC1-3, the simulation conditions in Steps 2 and 3 are identical. The different behavior of Sr diffusion and accumulation in IDZ and ASR_{ohm} increase is caused by the different barrier layer sintering temperatures applied in Step 1. Considering that the difference in the diffusion rate of Sr in DC1-3 is caused by the different microstructure at the IDZ after Step 1, the grain size can be selected as a microstructure indicator. Our calculated grain size of CGO after Step 1 is shown in Fig. 7b, representing an increasing trend from 0.15 μm at 1100 °C to 0.63 μm at 1400 °C, in good agreement with the experiment values[29]. In Fig. 7b, the effective interdiffusion coefficient of Sr in CeO_2 after the barrier sintering (Step 1) is estimated using Eq. (4) at both 1100 °C (the cathode-sintering temperature) and 800 °C (the long-term operation temperature). It can be clearly seen that the Sr diffusion slows down by a factor of about 10^5 when temperature decreases from 1100 to 800 °C, and the degree of interdiffusion decreases when the barrier sintering temperature (T_{Step1}) increase. That is to say that the higher sintering temperature in Step 1 can result in larger grain size in IDZ, better prevention of Sr diffusion, and thus less SZO formation.

However, based on the current simulation result, the thicker IDZ shown in Fig. 7a generated at higher sintering temperature can lead to a significant increase of ASR_{ohm}, e.g., DC3. So both of the two variables, i.e., the thickness of IDZ and diffusion of Sr in CGO, shown in Fig. 7a, b have a complex influence on the formation of SZO and the resulting ASR_{ohm} increase, which should be carefully controlled to reach optimum cell performance. In the case of PLD CGO barrier layer, the absence of Step 1 avoids the formation of

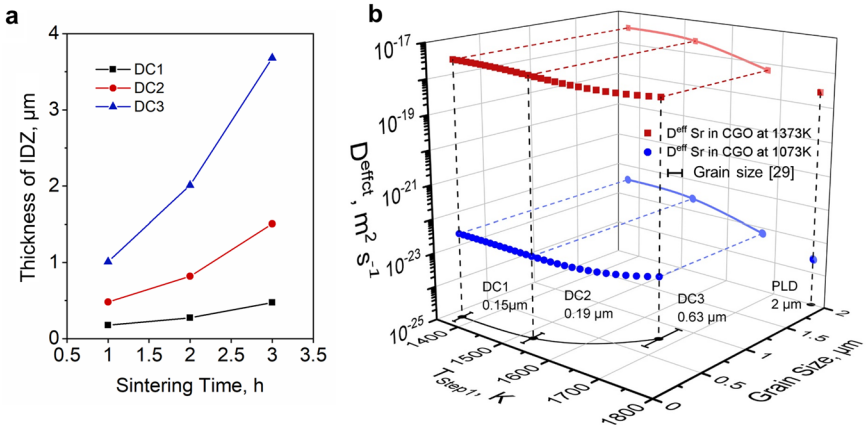

Fig. 7 Numerical analysis on changes of the microstructural parameters during the oxygen electrode–electrolyte interface reactions. **a** Simulated IDZ thickness for DC1, DC2, and DC3 after the barrier sintering step at 1100, 1250, and 1400 °C. **b** The estimated effective interdiffusion coefficient of Sr in CeO_2 barrier layer at 1073 K and 1373 K plotted against the sintering temperature of Step 1 and the corresponding grain size of CGO. The solid lines show the general trend and the dashed lines are to aid figure analysis. The error bars show the range of measured grain size reported in literature[29].

thick IDZ, and the large CGO grain size of ~2 μm results in about ten times slower Sr diffusion than that in screen-printed CGO, as shown in Fig. 7b. Together with the thin PLD CGO layer, the current simulation gives an ASR_{ohm} below 100 mΩ cm^2, as shown in Fig. 4c. In spite of the advantages of the PLD CGO barrier layer, the screen-printed CGO layer remains the most economic and promising method for the purpose of commercialization. In such case, the current work gives a technical route of computational aided optimization of cell fabrication conditions for the oxygen electrode–electrolyte interface and also a model to predict cell degradation in solid oxide fuel cells.

In summary, models are developed to reproduce the YSZ–CGO interdiffusion and the SZO formation at the YSZ–CGO interface in this work. The YSZ–CGO–LSCF system is simplified to the ZrO_2–CeO_2–SrO system, accounting for interdiffusion of the major elements (Zr and Ce) and the transportation of Sr from LSCF and reaction with YSZ forming SZO. The CALPHAD-type thermodynamic and diffusion kinetic information of the ZrO_2–CeO_2–SrO system is carefully evaluated and used as unique input to all the numerical modeling. Our 1D and 3D models reproduce the experimentally observed element distribution and microstructure evolution during the relevant steps in cell production and operation, for both screen-printed and PLD CGO barrier layers, indicating the credibility of our model. The calculated ASR_{ohm} suggests a trackable performance evolution within the oxygen electrode–electrolyte interface during the entire fabrication and long-term operation of SOFCs with the help of computational materials modeling. The two key factors of the cell degradation, i.e., IDZ caused by CGO–YSZ interdiffusion and Sr diffusion induced SZO formation, are analyzed to be strongly dependent on the fabrication condition of CGO barrier layer and a trade-off should be made when choosing the optimum processing route. It is expected the current route of computer engineering of the oxygen electrode–electrolyte interface in solid oxide fuel cells can serve as quantitative guide to the selection of fabrication conditions and prediction of cell degradation.

METHODS

Construction of thermodynamic and diffusion kinetic database

One set of CALPHAD-type thermodynamic and diffusion kinetic databases is constructed and applied as the accurate numerical input for all the simulations performed in this work. The basic idea of CALPHAD approach is to describe the thermodynamic properties of each phase in a system with a mathematical model containing adjustable parameters, which can be evaluated by the optimization method to fit the model to all available experimental information. It is then possible to calculate phase diagrams as well as thermodynamic properties of all the phases[35]. The compound energy formalism (CEF)[36] is widely used in CALPHAD modeling, which is introduced here to describe the Gibbs energy for the phases in the current YSZ–CGO–LSCF system. The general formula of a Gibbs free energy function ${}^0G(T) = G(T) - H^{SER}$ (lattice stability) for stoichiometric compounds can be expressed as,

$$ {}^0G^i(T) = A_i + B_iT + C_iT\,ln(T) + D_iT^2 + E_iT^{-1} + F_iT^7 + G_iT^{-9} \quad (1) $$

where H^{SER} is the weighted molar enthalpy of the stable element reference (SER), the pure element in its stable state at 298.15 K, and T the absolute temperature. The subscript i represents the phase described and $A_i \sim F_i$ are parameters to be optimized. There are nine elements included in the current YSZ–CGO–LSCF system, i.e., Zr–Y–Ce–Gd–La–Sr–Co–Fe–O, and it is an extensive project to establish the thermodynamic database for the entire nine-element system, which is also unnecessary for the current simulation.

In the current work, the YSZ–CGO–LSCF system is simplified to a model system of ZrO_2–CeO_2–SrO. Specifically, the interdiffusion between YSZ and CGO can be simplified to the generation of interdiffusion zone (IDZ) between cubic ZrO_2 and CeO_2, where the two boundaries of IDZ are defined when detecting 0.1 at. % ZrO_2 on the CeO_2-rich side or 0.1 at. % CeO_2 dissolved in the ZrO_2 part. The cubic ZrO_2 and CeO_2 phases can be thermodynamically treated as a single Cubic phase following our previous simulation result[33,34]. We then use SrO to represent the LSCF perovskite that provides Sr^{2+} (or Sr) to react with ZrO_2 in IDZ. Such a simplification can reasonably and sufficiently account for the main purpose of studying the interdiffusion between YSZ and CGO, the diffusion of Sr^{2+} (or Sr) through the CGO layer, and the formation of SZO at the YSZ–CGO interface. The end-members of the current ZrO_2–CeO_2–SrO system will then be used to represent the corresponding component in the YSZ–CGO–LSCF system in the kinetic modeling. The lattice stabilities of the Cubic, SrO, and SZO phases are taken from previous thermodynamic modeling[37–39], and are carefully evaluated to construct the current thermodynamic database as described in Supplementary Methods. No higher-order parameter is used except for the Cubic phase, in order to describe their mutual solid solubility. The molar Gibbs energy of the cubic phase can be described as,

$$ \begin{aligned} G_m^{Cubic} = {} & c^0_{(Zr^{4+})_1(O^{2-})_2} G^{Cubic}_{(Zr^{4+})_1(O^{2-})_2} + c^0_{(Ce^{4+})_1(O^{2-})_2} G^{Cubic}_{(Ce^{4+})_1(O^{2-})_2} \\ & + RT\left(c_{(Zr^{4+})_1(O^{2-})_2} lnc_{(Zr^{4+})_1(O^{2-})_2} + c_{(Ce^{4+})_1(O^{2-})_2} lnc_{(Ce^{4+})_1(O^{2-})_2} \right) \\ & + c_{(Zr^{4+})_1(O^{2-})_2} c^0_{(Ce^{4+})_1(O^{2-})_2} L^{Cubic} \end{aligned} \quad (2) $$

where R is the gas constant, ${}^{0}L^{\mathrm{Cubic}}$ is the interaction parameter, $c_{(Zr^{4+})(O^{2-})_2}$ and $c_{(Ce^{4+})(O^{2-})_2}$ are the mole fraction of cubic ZrO_2 and CeO_2, respectively. The thermodynamic description of the ZrO_2–CeO_2–SrO system is listed in Table 1, where the sublattice model with charged species is adopted.

The diffusion of Ce and Zr between CGO and YSZ can be treated as in our previous work[33,34]. On the other hand, the Sr migration through CGO layer is rather complex, and different mechanisms have been proposed in the literature, including gas-phase diffusion through the pore phase, surface diffusion, or bulk/grain boundary diffusion[40,41]. For the gas-phase diffusion, it is generally believed that SrO derived from the strontium segregation in LSCF reacts with water vapor to form the volatile $Sr(OH)_2$ gas species, and afterward transports in the vapor form and deposits again at the reactive sites as SrO. The fast surface diffusion indicates the transport of Sr^{2+} (or Sr) along the crack wall or the inner surface in the CGO barrier, while the bulk/grain boundary diffusion driven by the chemical potential of Sr^{2+} (or Sr) appears to be slower, especially for the bulk diffusion which is significantly slower than the other diffusion mechanisms. These different diffusion mechanisms play different roles, depending on the experimental conditions, such as porosity of the CGO barrier layer, temperature, $P(O_2)$, and $P(H_2O)$, etc. However, there is still a lack of experimental proof and quantification in the literature on how the different diffusion mechanisms contribute to the overall Sr diffusion. In this work, instead of quantitatively distinguishing the contributions from different diffusion mechanisms or the form of Sr to transport (as gas species, neutral atoms, or cations) which is more or less impossible based on available experimental information, we developed a quantitative description of the overall Sr^{2+} migration and SZO formation by using an "apparent" diffusion coefficient. In terms of the diffusion kinetic data, the Arrhenius expression is sufficient to describe the temperature dependence of diffusivity of each charged species in different phases, i.e.,

$$D(T) = D_0 \cdot \exp\left(\frac{-Q}{RT}\right) \tag{3}$$

where D_0 is the prefactor and Q is the activation energy. The elemental diffusivity data of the current ZrO_2–CeO_2–SrO system evaluated using previous experimental data[42–45] are listed in Table 2, presented as the CALPHAD-type atomic mobility functions as input data for the current 1D simulation. The methodologies to evaluate atomic mobility and the quality of resulting parameters are detailed in Supplementary Methods, Supplementary Fig. 2a–d and Supplementary Table 1. In the current database, the "effective" diffusivity formulated as Hart's equation[46] is used, which consists of two contributing items corresponding to the bulk and grain boundary (gb) diffusion, respectively. As shown in Eq. (4), the grain boundary item is used to account for the faster Sr migration via grain boundary, surface, and vapor diffusion without further distinguishing between them, due to lack of precise experimental information.

$$D^{\mathrm{effect}} = \frac{\delta}{d} \cdot D^{\mathrm{gb}} + \left(1 - \frac{\delta}{d}\right) \cdot D^{\mathrm{bulk}} \tag{4}$$

where δ and d are the grain boundary thickness and the grain size, respectively. As for δ, a nominal value of 5–10 atomic diameter is suggested as in ref. [47], and δ is thus assumed to be 1 nm in the current simulation. As for d, only the grain growth in the CGO layer is included in the present database due to the model of 1D simulation, which will be described in detail in the modeling part. The sintering temperature for the YSZ electrolyte layer is in general a few hundred degrees higher than that of CGO. We hence assume no grain growth in the YSZ layer during sintering of barrier layer and cathode and during long-term operation (Steps 1–3 in Fig. 1). Previous studies[48–50] performed systematic experimental investigations on the grain growth behavior of the CGO system as functions of temperature and time, and proposed the following analytical equation,

$$d^2 = d_0^2 + K_0 t \exp\left(\frac{-Q_g}{RT}\right) \tag{5}$$

where d is the average grain size at time t, d_0 is the initial grain size, K_0 is a pre-exponential constant, R is the gas constant, T is the absolute temperature, and Q_g denotes the activation energy for grain growth. According to the previous work[50], the parameters in our simulation are set to be $d_0 = 1.5 \times 10^{-7}$ m, $K_0 = 0.04\ \mathrm{m^2\,s^{-1}}$ and $Q_g = 477\ \mathrm{kJ\,mol^{-1}}$, respectively.

1D kinetic modeling

As the current YSZ–CGO–LSCF system is simplified to the ZrO_2–CeO_2–SrO model system, the phase relations can be computed based on the current thermodynamic description listed in Table 1[51]. Figure 8a shows the calculated isothermal section of the ZrO_2–CeO_2–SrO system at 1523 K. The SZO phase is located in the middle of the ZrO_2–SrO binary line, while a miscibility gap between cubic ZrO_2 and CeO_2 can be found on the ZrO_2–CeO_2 side. This miscibility gap of the phase Cubic extends to the ZrO_2–SrO side to reach a two-phase equilibrium with the SZO phase.

We first construct the 1D numerical model to simulate the elemental interdiffusion and formation of SZO in the ZrO_2-CeO_2-SrO system, considering different methods for fabricating the barrier layers, i.e., the screen-printed CGO and PLD CGO. Figure 8b gives the 1D numerical model in the case of the screen-printed CGO barrier layer. The three-step (Steps 1–3) simulation is in correspondence to the three processes described in Fig. 1. In order to guarantee the comparability of the current simulation results with previous experimental data, the simulation conditions are set according to the experimental work[24]. In Step 1, the initial thickness of ZrO_2 and CeO_2 layer is set to be 8 and 6 μm, respectively, representing the initial YSZ electrolyte and the CGO barrier layer. The sintering temperature and time are set to be 1523 K and 2 h. The grain growth in CeO_2 region should be considered due to the dramatic increase in grain size during barrier layer sintering at high temperature[24,48–50], which has a strong influence on the elemental diffusion behavior[29]. The reason for no grain growth considered in the ZrO_2 layer is that the YSZ electrolyte layer has been pre-sintered at ~1673 K[28], resulting in quite a large grain size. Co-sintering together the CGO barrier layer at 1523 K will thus not lead to significant grain growth in the YSZ layer. Grain size of 2 μm is adopted for the ZrO_2 region in our model. At the right boundary of the CeO_2 region (Fig. 8b), the appearance of LSCF cathode is represented by a virtual SrO layer with no thickness and one boundary condition on the activity of SrO phase (a(SrO)), which is set to be 0 in Step 1. In Step 2, i.e., the cathode-sintering process, the a(SrO) is then set to be 1 and the simulation condition is set to be at 1373 K for 2 h. The grain growth in the CeO_2 region should still be considered in this step. During long-term operation, i.e., Step 3, the grain growth in CeO_2 region is ignored due to the low operating temperature at 973 K. The simulation time is selected to be 2000 h to be the same as reported in ref. [24].

Figure 8c gives the 1D numerical model in the case of the PLD CGO barrier layer. The simulation conditions are the same as in the reported experimental work[16]. A CeO_2 barrier layer (representing CGO) with a thickness of 0.6 μm is placed on the right side of the ZrO_2 region (8 μm, representing YSZ). Since the PLD CGO barrier layer exhibits an epitaxy microstructure, the grain size of CeO_2 is set to be identical to that of ZrO_2 i.e., 2 μm. The deposition of the PLD CGO layer requires no further high-

Table 1. Thermodynamic description of the ZrO_2–CeO_2–SrO system adopted in this work.

Phase	Description	Reference
Cubi $(Ce^{4+},Zr^{4+})_1(O^{2-})_2$	${}^{0}G^{\mathrm{Cubic}}_{(Zr^{4+})_1(O^{2-})_2} = -1125234.1 + 496.72262T - 80TlnT$ ${}^{0}G^{\mathrm{Cubic}}_{(Ce^{4+})_1(O^{2-})_2} = -1116114 + 429.345T - 72.0653TlnT - 0.0040536T^2 + 0.0040536T^{-1}$ ${}^{0}L^{\mathrm{Cubic}} = 27797.69$	37
SrO $(Sr^{2+})_1(O^{2-})_1$	${}^{0}G^{\mathrm{SrO}} = -607870 + 268.9T - 47.36TlnT - 0.00307T^2 + 190000T^{-1}$	38
SZO $(Sr^{2+})_1(Zr^{4+})_1(O^{2-})_3$	${}^{0}G^{\mathrm{SZO}} = -1809275.23 + 733.05819T - 124.65927TlnT - 0.0029230815T^2 + 1026060.9T^{-1}$	39

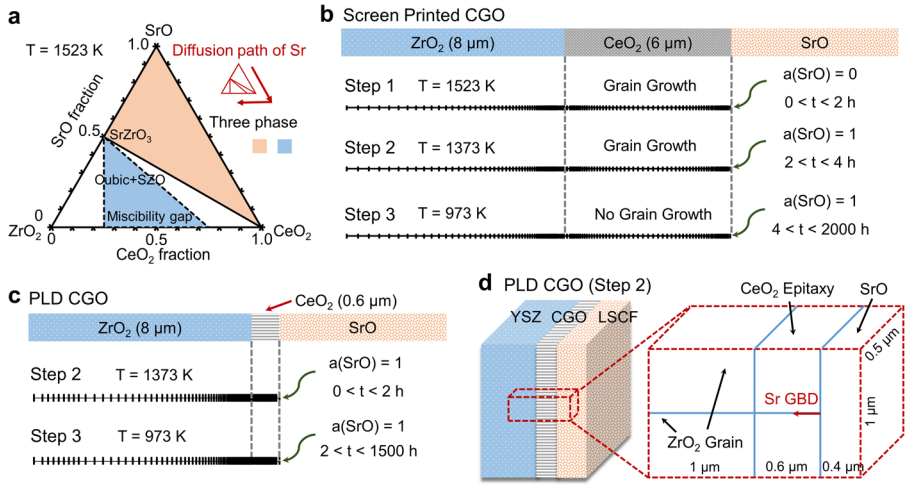

Fig. 8 Models developed for simulating the oxygen electrode–electrolyte interface reactions. a Calculated isothermal section of the ZrO_2–CeO_2–SrO system at 1523 K. **b** 1D numerical model for the simulation of the ZrO_2–CeO_2–SrO system in the case of screen-printed CGO barrier layer. **c** 1D numerical model for the simulation of the ZrO_2-CeO_2-SrO system in the case of PLD CGO barrier layer. **d** Numerical model for 3D phase-field simulation of the SZO formation in the case of PLD CGO barrier layer. For (**b**) and (**c**), the SrO layer is introduced as a virtual layer without thickness.

Table 2. The elemental diffusivity data of the current ZrO_2–CeO_2–SrO system evaluated based on previous experimental data[42–45].

Diffusion component	D_0^{bulk} ($m^2\,s^{-1}$)	Q^{bulk} ($kJ\,mol^{-1}$)	D_0^{gb} ($m^2\,s^{-1}$)	Q^{gb} ($kJ\,mol^{-1}$)
Zr^{4+} in YSZ[a]	4.1×10^{-6}	−434.2	4.1×10^{-6}	−286.9
Ce^{4+} in YSZ	4.0×10^{-4}	−516.0	4.0×10^{-4}	−403.4
Sr^{2+} in YSZ[b]	8.9×10^{-4}	−601.5	8.9×10^{-4}	−466.1
Zr^{4+} in CGO[a]	9.8×10^{-4}	−518.4	9.8×10^{-4}	−375.1
Ce^{4+} in CGO[c]	4.0×10^{-4}	−516.0	4.0×10^{-4}	−403.4
Sr^{2+} in CGO	8.9×10^{-4}	−601.5	8.9×10^{-4}	−466.1

[a]Due to lack of experimental data, the grain boundary diffusivity is assumed to be 10^5 times higher than the bulk diffusivity.
[b]Diffusivity of Sr^{2+} in YSZ is assumed to be the same as in CGO due to lack of experimental data.
[c]Diffusivity of Ce^{4+} in CGO is assumed to be the same as in YSZ due to lack of experimental data.

temperature heat treatment (sintering) afterward. In this case, only two processing steps are considered in our simulation, i.e., Step 2—Cathode sintering and Step 3—Long-term operation. The simulation conditions are set to be 1373 K for 2 h and 973 K for 1500 h, for Steps 2 and 3, respectively. Similar to the case of screen-printed CGO, the CGO grain growth is considered during the cathode-sintering step, and the boundary condition of $a(\mathrm{SrO}) = 1$ is applied to represent the presence of the LSCF cathode. The current 1D numerical model is also used to reproduce the change of volume percentage of SZO in IDZ during long-term operation for up to 10,700 h determined by focused ion beam-scanning electron microscopy (FIB-SEM) serial sectioning (Fig. 3)[28], as well as to estimate the effect of barrier layer sintering temperature on the ohmic loss to compare with the previously reported data (Figs. 6 and 7)[29]. In these cases, the modeling parameters (i.e., thickness of YSZ and CGO, temperature, time, etc.) are adjusted according to different experimental conditions adopted in the previous work[28,29].

In this work, the above numerical kinetic modeling is carried out using the DICTRA software package implemented in Thermo-Calc[51]. The homogenization model[52] in DICTRA is activated to reveal a good coupling between thermodynamic and diffusion kinetic information in Tables 1 and 2. The non-uniform grid is sufficiently refined close to the ZrO_2–CeO_2 interface region and the right boundary of the CeO_2 region to guarantee numerical stability during simulation, as illustrated in Fig. 8b, c. It should be further pointed out that due to the simplification of using an apparent diffusion coefficient to represent the Sr migration, i.e., Eq. (4), in this paper, we refer Sr diffusion all in the form of Sr^{2+} irrespective of the different diffusion mechanisms. The different "effective" diffusion behavior of Sr^{2+} for the 1D cases of screen-printed CGO and PLD CGO is reproduced by considering the evolution of grain size, with no further consideration on the change of porosity. Meanwhile, the current model only includes the effect of temperature and time in the simulation of Sr^{2+} migration and SZO formation during the 1D long-term operation stage. The effect of electric boundary conditions on the local $P(O_2)$ at the oxygen electrode–electrolyte interface is not considered in the current frame of calculation, since it would lead to the complex phenomenon of simultaneous anion and cation migration induced by both electric and chemical potential gradient, with thermodynamic and kinetic phase transformation due to element redistribution[53]. This is also based on considerations that in reality, the temperature has an even bigger effect than $P(O_2)$ simply due to fast diffusion kinetics at elevated temperatures. These simplifications adopted in current modeling may cause deviation from experimental data, and continuous efforts are being made to include more variables of real conditions in our future computational engineering studies.

3D phase-field modeling

Apart from 1D simulation, the current work takes advantage of the multiphase field model[54,55] to simulate microstructure evolution and SZO formation in the case of the PLD CGO barrier layer. Comparing with the 1D DICTRA simulation, which is suitable for the simulation of SZO formation on a very large time scale, the phase-field simulation mainly focuses on reproducing the details of microstructure evolution within a short period of time. Since the phase-field simulation is computationally expensive, in this work, it is employed only to describe the SZO formation and growth during Step 2 in the case of the PLD CGO layer. In the multiphase field theory, each phase grain α is distinct from the other phases by its individual phase field ϕ_α. Three phases are considered in the current ZrO_2-CeO_2-SrO model system, i.e., the Cubic, SrO, and SZO phases. The sum constrain exists as $\sum_{\alpha=1\ldots3}\phi_\alpha = 1$. The governing equation for each phase-field can be

expressed as,

$$\dot{\phi}_a = \sum_{\beta=1\ldots N} \mu_{\alpha\beta}\left\{\sigma_{\alpha\beta}\left[\phi_\beta\nabla^2\phi_\alpha - \phi_\alpha\nabla^2\phi_\beta + \frac{\pi^2}{2\eta^2}(\phi_\alpha - \phi_\beta)\right] + \frac{\pi}{\eta}\sqrt{\phi_\alpha\phi_\beta}\Delta g_{\alpha\beta}\right\} \quad (6)$$

where $\mu_{\alpha\beta}$ is the interfacial mobility, $\sigma_{\alpha\beta}$ is the interfacial energy, $\Delta g_{\alpha\beta}$ is the local deviation from thermodynamic equilibrium and η is the interface thickness. Evolution of the conserved composition field c_α is coupled to phase-field and is governed by,

$$\dot{c}_\alpha = \nabla \cdot \sum_{\alpha=1\ldots N} \phi_\alpha D_\alpha^{tot} \nabla c_\alpha \quad (7)$$

Figure 8d shows the computational domain in our SZO formation model using the phase-field method. The cathode-sintering step (Step 2) in the case of the PLD CGO barrier is selected here to study the typical microstructure evolution during formation of SZO phase at the quadruple junction. Considering the grain size of the YSZ phase and the thickness of the CGO layer in the experimental work[16], a cuboid region of $2 \times 1 \times 0.5$ μm is modeled including three layers of ZrO_2 (1 μm), CeO_2 (0.6 μm), and SrO (0.4 μm) from the left to the right side. Grain boundaries are defined in the middle of the ZrO_2 and CeO_2 region forming a quadruple junction to keep consistent with the experimentally observed CGO epitaxy[16]. The current 3D modeling is carried out using MICRESS (http://www.micress.de.), and the grain boundary diffusion model is activated to detect the faster Sr diffusion along CGO grain boundary and the formation of SZO at the quadruple junction. Under such circumstances, the total diffusivity D_α in Eq. (7) should contain an extra flux contributed by grain boundary diffusion, i.e.,

$$D_\alpha^{tot} = D_\alpha^{bulk} + D_\alpha^{gb} \quad (8)$$

where D_α^{bulk} and D_α^{gb} are bulk and grain boundary diffusivities with the prefactor and activation energy shown in Table 2. It should be noted that D_α^{gb} contributes to D_α^{tot} only at the phase interface since it is also proportional to $\phi_\alpha\phi_\beta$ and will cancel out in the bulk region. In order to allow for the formation of the SZO phase, the seed density model[56] is applied by placing randomly distributed inactive SZO particles in the simulation area with an initial grain radius of 0. The SZO particles at the quadruple junction can be stabilized when a sufficient amount of Sr is accumulated to reach the two-phase equilibrium with the Cubic phase as shown in Fig. 8a.

In this work, $\Delta g_{\alpha\beta}$ and D_α can be directly obtained from the thermodynamic and diffusion kinetic database developed for the ZrO_2–CeO_2–SrO system, as shown in Tables 1 and 2. Integration of these currently developed thermodynamic and diffusion databases into the 3D phase-field model can be revealed owning to the good coupling between Themo-calc and MICRESS[51,56]. For simplification, all the phases/grains were assumed to be isotropic. The interface mobility $\mu_{\alpha\beta}$ for the CGO and YSZ grain boundaries are acquired from literature to be 1.7×10^{-8} and 6.5×10^{-10} $cm^4\,J^{-1}\,s^{-1}$, respectively[57,58]. And the interface energy $\sigma_{\alpha\beta}$ for both of the CGO and YSZ grain boundaries are set to 3.0×10^{-5} $J\,cm^{-2}$ as reported in literature[57,58]. The interface thickness η is set to be 3×10^{-8} m. For all the other interfaces with no experimental data available, $\mu_{\alpha\beta}$ and $\sigma_{\alpha\beta}$ are adjusted to be 1.0×10^{-10} $cm^4\,J^{-1}\,s^{-1}$ and 2.0×10^{-5} $J\,cm^{-2}$ to simply reach diffusion control of the phase transformation.

Prediction of ohmic loss (ASR_{ohm})

The ohmic loss at the oxygen electrode–electrolyte interface of an SOFC cell can be ascribed to mainly the electrolyte resistance. In our simulation, an additional contribution to the ASR_{ohm} comes from both the YSZ–CGO IDZ and the SZO ion insulator. We consider an YSZ–CGO electrolyte region in 1D with a thickness of l, which is further split into n small grids. The theoretical ASR_{ohm} can be computed by simply summing up the resistivity of YSZ and CGO layer multiplied by each layer width. When the formation of IDZ and SZO is considered, the phase (volume) fraction and electrical resistance of cubic solid solution and SZO should be first computed separately within each grid. The electrical conductivity of a YSZ–CGO solid solution depending on composition and temperature can be found in previous experimental work[59], and the data at 700 and 800 °C fitted using polynomial equations are adopted in this work. The temperature-dependent conductivity of SZO has also been reported[60]. Then, we consider a parallel distributed cubic solid solution and SZO to calculate the effective resistivity $R(x)$ of each grid. The ohmic loss of the entire bi-layer electrolyte region is estimated by integrating $R(x)$ along the thickness as follow,

$$ASR_{ohm} = \int_0^l R(x)dx \approx \sum_1^n \frac{N_{Cubic}}{\sigma_{Cubic}}\frac{N_{SZO}}{\sigma_{SZO}} \Big/ \left(\frac{N_{Cubic}}{\sigma_{Cubic}} + \frac{N_{SZO}}{\sigma_{SZO}}\right)\Delta x \quad (9)$$

where σ_{Cubic} and σ_{SZO} are the electrical conductivity of cubic solid solution and SZO, respectively. N_{Cubic} and N_{SZO} are the phase fraction of cubic solid solution and SZO within each grid, which can be calculated based on the currently simulated composition profiles. In this work, the Ohmic loss is calculated based solely on the results of phase fraction obtained from Dictra 1D simulations of Steps 1–3 for both cases of the screen-printed and PLD CGO barrier layers.

DATA AVAILABILITY

The authors declare that the main data supporting the findings of this study are available within the paper. Other relevant data are available from the corresponding author upon reasonable request.

Received: 17 October 2020; Accepted: 29 June 2021;
Published online: 23 July 2021

REFERENCES

1. Menzler, N. H., Tietz, F., Uhlenbruck, S., Buchkremer, H. P. & Stöver, D. Materials and manufacturing technologies for solid oxide fuel cells. *J. Mater. Sci.* **45**, 3109–3135 (2010).
2. Kilner, J. A. & Burriel, M. Materials for intermediate-temperature solid-oxide fuel cells. *Annu. Rev. Mater. Res.* **44**, 365–393 (2014).
3. Jacobson, A. J. Materials for solid oxide fuel cells. *Chem. Mater.* **22**, 660–674 (2010).
4. Petric, A. Evaluation of La–Sr–Co–Fe–O perovskites for solid oxide fuel cells and gas separation membranes. *Solid State Ion.* **135**, 719–725 (2000).
5. Mai, A., Haanappel, V. A. C., Uhlenbruck, S., Tietz, F. & Stöver, D. Ferrite-based perovskites as cathode materials for anode-supported solid oxide fuel cells. *Solid State Ion.* **176**, 1341–1350 (2005).
6. Yamamoto, O. Perovskite-type oxides as oxygen electrodes for high temperature oxide fuel cells. *Solid State Ion.* **22**, 241–246 (1987).
7. Marinha, D., Dessemond, L. & Djurado, E. Comprehensive review of current developments in IT-SOFCs. *Curr. Inorg. Chem.* **3**, 2–22 (2013).
8. Wand, W. & Mogensen, M. High-performance lanthanum-ferrite-based cathode for SOFC. *Solid State Ion.* **176**, 457–462 (2005).
9. Tu, H. & Stimming, U. Advances, aging mechanisms and lifetime in solid-oxide fuel cells. *J. Power Sources* **127**, 284–293 (2004).
10. Simner, S. P., Anderson, M. D., Engelhard, M. H. & Stevenson, J. W. Degradation mechanisms of La–Sr–Co–Fe–O_3 SOFC cathodes. *Electrochem. Solid-State Lett.* **9**, A478 (2006).
11. Yokokawa, H. et al. Thermodynamic and kinetic considerations on degradations in solid oxide fuel cell cathodes. *J. Alloy. Compd.* **452**, 41–47 (2008).
12. Komatsu, T., Chiba, R., Arai, H. & Sato, K. Chemical compatibility and electrochemical property of intermediate-temperature SOFC cathodes under Cr poisoning condition. *J. Power Sources* **176**, 132–137 (2008).
13. Mai, A. et al. Time-dependent performance of mixed-conducting SOFC cathodes. *Solid State Ion.* **177**, 1965–1968 (2006).
14. Martínez-Amesti, A. et al. Reactivity between La(Sr)FeO_3 cathode, doped CeO_2 interlayer and yttria-stabilized zirconia electrolyte for solid oxide fuel cell applications. *J. Power Sources* **185**, 401–410 (2008).
15. Uhlenbruck, S., Moskalewicz, T., Jordan, N., Penkalla, H. J. & Buchkremer, H. P. Element interdiffusion at electrolyte-cathode interfaces in ceramic high-temperature fuel cells. *Solid State Ion.* **180**, 418–423 (2009).
16. Knibbe, R. et al. Cathode-electrolyte interfaces with CGO barrier layers in SOFC. *J. Am. Ceram. Soc.* **93**, 2877–2883 (2010).
17. Horita, T. et al. Ceria-zirconia composite electrolyte for solid oxide fuel cells. *J. Electroceram.* **1**, 155–164 (1997).
18. Tu, H. Y., Takeda, Y., Imanishi, N. & Yamamoto, O. Electrode in solid oxide fuel cells. *Solid State Ion.* **117**, 277–281 (1999).
19. Uchida, H. High performance electrode for medium-temperature solid oxide fuel cells La(Sr)CoO_3 cathode with ceria interlayer on zirconia electrolyte. *Electrochem. Solid-State Lett.* **2**, 428 (2002).
20. Tsoga, A., Gupta, A., Naoumidis, A. & Nikolopoulos, P. Gadolinia-doped ceria and yttria stabilized zirconia interfaces: regarding their application for SOFC technology. *Acta Mater.* **48**, 4709–4714 (2000).
21. Mitsuyasu, H. Analysis of solid state reaction at the interface of yttria-doped ceria/yttria-stabilized zirconia. *Solid State Ion.* **113–115**, 279–284 (2002).

22. Wang, F. et al. Sr and Zr diffusion in LSCF/10GDC/8YSZ triplets for solid oxide fuel cells (SOFCs). *J. Power Sources* **258**, 281–289 (2014).
23. Jordan, N. et al. $Ce_{0.8}Gd_{0.2}O_{2-\delta}$ protecting layers manufactured by physical vapor deposition for IT-SOFC. *Solid State Ion.* **179**, 919––923 (2008).
24. Kiebach, R. et al. Stability of $La_{0.6}Sr_{0.4}Co_{0.2}Fe_{0.8}O_3/Ce_{0.9}Gd_{0.1}O_2$ cathodes during sintering and solid oxide fuel cell operation. *J. Power Sources* **283**, 151–161 (2015).
25. Szasz, J. et al. High-Performance Cathode/Electrolyte Interfaces for SOFC. *ECS Trans.* **68**, 763–771 (2015).
26. Wankmüller, F. et al. Correlative tomography at the cathode/electrolyte interfaces of solid oxide fuel cells. *J. Power Sources* **360**, 399–408 (2017).
27. Matsuda, J. et al. TEM and ETEM study on $SrZrO_3$ formation at the LSCF/GDC/YSZ interfaces. *ECS Trans.* **78**, 993–1001 (2017).
28. Rinaldi, G. et al. Strontium migration at the GDC-YSZ interface of solid oxide cells in SOFC and SOEC modes. *ECS Trans.* **78**, 3297–3307 (2017).
29. Wilde, V. et al. $Gd_{0.2}Ce0.8O_2$ diffusion barrier layer between $(La_{0.58}Sr_{0.4})(Co_{0.2}Fe_{0.8})O_{3-\delta}$ cathode and $Y_{0.16}Zr_{0.84}O_2$ electrolyte for solid oxide fuel cells: effect of barrier layer sintering temperature on microstructure. *ACS Appl. Energy Mater.* **1**, 6790–6800 (2018).
30. Chou, J.-T. et al. Mechanism of $SrZrO_3$ formation at GDC/YSZ interface of SOFC cathode. *J. Electrochem. Soc.* **165**, F959–F965 (2018).
31. Railsback, J., Choi, S. H. & Barnett, S. A. Effectiveness of dense Gd-doped ceria barrier layers for $(La,Sr)(Co,Fe)O_3$ cathodes on Yttria-stabilized zirconia electrolytes. *Solid State Ion.* **335**, 74–81 (2019).
32. Zhang, Y. et al. Recent progress on advanced materials for solid-oxide fuel cells operating below 500 °C. *Adv. Mater.* **29**, 1700132 (2017).
33. Xu, H. et al. Interdiffusion between gadolinia doped ceria and yttria stabilized zirconia in solid oxide fuel cells: experimental investigation and kinetic modeling. *J. Power Sources* **441**, 227152 (2019).
34. Cheng, K. et al. Numerical simulation of the $SrZrO_3$ formation in solid oxide fuel cells. *J. Electron. Mater.* **48**, 5510–5515 (2019).
35. Lukas, H., Fries, S. G. & Sundman, B. *Computational Thermodynamics: The Calphad Method* (Cambridge University Press, 2007).
36. Hillert, M. The compound energy formalism. *J. Alloy. Compd.* **320**, 161–176 (2001).
37. Du, Y., Yashima, M., Koura, T., Kakihana, M. & Yoshimura, M. Thermodynamic evaluation of the ZrO_2-CeO_2 system. *Scr. Metall. Mater.* **31**, 327–332 (1994).
38. Risold, D., Hallstedt, B. & Gauckler, L. J. The Strontium-oxygen system. *Calphad Comput. Coupling Phase Diagr. Thermochem* **20**, 353–361 (1996).
39. Gong, W. P. et al. Experimentation and thermodynamic modelling on $SrZrO_3$. *Trans. Nonferrous Met. Soc. China* **17**, 739–743 (2007)..
40. Lu, Z. et al. $SrZrO_3$ formation at the interlayer/electrolyte interface during $(La_{1-x}Sr_x)_{1-\delta}Co_{1-y}FeyO_3$ cathode sintering. *J. Electrochem. Soc.* **164**, F3097–F3103 (2017).
41. Darvish, S., Gopalan, S. & Zhong, Y. Thermodynamic stability maps for the $La_{0.6}Sr_{0.4}Co_{0.2}Fe_{0.8}O_{3\pm\delta}$–$CO_2$–$O_2$ system for application in solid oxide fuel cells. *J. Power Sources* **336**, 351–359 (2016).
42. Kilo, M. et al. Cation transport in yttria stabilized cubic zirconia: ^{96}Zr tracer diffusion in $(Zr_xY_{1-x})O_{2-x/2}$ single crystals with $0.15 \leqslant x \leqslant 0.48$. *J. Eur. Ceram. Soc.* **20**, 2069–2077 (2000).
43. Bekale, V. M., Huntz, A. M., Legros, C., Sattonnay, G. & Jomard, F. Impurity diffusion of cerium and gadolinium in single- and polycrystalline yttria-stabilized zirconia. *Philos. Mag.* **88**, 1–19 (2008).
44. Beschnitt, S. & De Souza, R. A. Impurity diffusion of Hf and Zr in Gd-doped CeO_2. *Solid State Ion.* **305**, 23–29 (2017).
45. Mandt, T. et al. Sr-diffusion in $Ce_{0.8}Gd_{0.2}O_{2-\delta}$ layers for SOFC application. *Mater. Res. Soc. Symp. Proc.* **1542**, 26–31 (2013).
46. Hart, E. W. On the role of dislocations in bulk diffusion. *Acta Met.* **5**, 597 (1957).
47. German, R. M. *Thermodynamic and Kinetic Treatments. Sintering: From Empirical Observations to Scientific Principles* (Elsevier, 2014).
48. He, Z. et al. Densification and grain growth during early-stage sintering of $Ce_{0.9}Gd_{0.1}O_{1.95-\delta}$ in a reducing atmosphere. *Acta Mater.* **58**, 3860–3866 (2010).
49. Ni, D. W. et al. Densification and grain growth during sintering of porous $Ce_{0.9}Gd_{0.1}O_{1.95}$ tape cast layers: a comprehensive study on heuristic methods. *J. Eur. Ceram. Soc.* **33**, 2529–2537 (2013).
50. Ni, D. W., Esposito, V., Foghmoes, S. P. V. & Ramousse, S. Densification and grain growth kinetics of $Ce_{0.9}Gd_{0.1}O_{1.95}$ in tape cast layers: the influence of porosity. *J. Eur. Ceram. Soc.* **34**, 2371–2379 (2014).
51. Andersson, J.-O., Helander, T., Höglund, L., Shi, P. & Sundman, B. Thermo-Calc & DICTRA, computational tools for materials science. *Calphad* **26**, 273–312 (2002).
52. Larsson, H. & Höglund, L. Multiphase diffusion simulations in 1D using the DICTRA homogenization model. *Calphad* **33**, 495–501 (2009).
53. Ta, N. et al. Numerical simulation of kinetic demixing and decomposition in a $LaCoO_{3-\delta}$ oxygen membrane under an oxygen potential gradient. *J. Memb. Sci.* **548**, 526–539 (2018).
54. Steinbach, I. et al. A phase field concept for multiphase systems. *Phys. D. Nonlinear Phenom.* **94**, 135–147 (1996).
55. Steinbach, I. Phase-field models in materials science. *Model. Simul. Mater. Sci. Eng.* **17**, 073001 (2009).
56. Bottger, B., Eiken, J. & Steinbach, I. Phase field simulation of equiaxed solidification in technical alloys. *Acta Mater.* **54**, 2697–2704 (2006).
57. Chen, P. L. & Chen, I. W. Grain growth in CeO_2: dopant effects, defect mechanism, and solute drag. *J. Am. Ceram. Soc.* **79**, 1793–1800 (1996).
58. Dong, Y. & Chen, I. Mobility transition at grain boundaries in two-step sintered 8 mol% yttria-stabilized zirconia. *J. Am. Ceram. Soc.* **101**, 1857–1869 (2018).
59. Tsoga, A. Total electrical conductivity and defect structure of ZrO_2–CeO_2–Y_2O_3–Gd_2O_3 solid solutions. *Solid State Ion.* **135**, 403–409 (2000).
60. Willy Poulsen, F. & van der Puil, N. Phase relations and conductivity of Sr- and La-zirconates. *Solid State Ion.* **53–56**, 777–783 (1992).

ACKNOWLEDGEMENTS

This work is supported by European Horizon 2020-Research and Innovation Framework Programme (H2020-JTI-FCH-2015-1) under grant agreement No.735918 (INSIGHT project) and by EUDP through project no. 64017-0011 (EP2Gas). In addition, the National Natural Science Foundation of China (Nos. 51801116 and 52001176), Shandong Province Key Research and Development Plan (Nos. 2019GHZ019, 2019JZZY010364, and 2019JZZY020329) and the Youth Innovation and Technology Support Program of Shandong Provincial Colleges and Universities (No. 2020KJA002) are acknowledged. The authors would like to acknowledge Dr. Arata Nakajo and Dr. Giorgio Rinaldi from EPFL for providing the original FIB-SEM data and fruitful discussion.

AUTHOR CONTRIBUTIONS

K.C. and H.X. contributed equally to the work on the methodology, software, formal analysis and writing of the original draft. L.Z. and Y.D. provided the datasets and contributed to the writing and to the formal analysis. J.Z. and X.W. were responsible for writing and funding acquisition. M.C. conceived and coordinated the research project and was responsible for supervision, writing, and funding acquisition. All authors reviewed the final manuscript.

COMPETING INTERESTS

The authors declare no competing interests.

ADDITIONAL INFORMATION

Supplementary information The online version contains supplementary material available at https://doi.org/10.1038/s41524-021-00584-8.

Correspondence and requests for materials should be addressed to J.Z. or M.C.

Reprints and permission information is available at http://www.nature.com/reprints

Publisher's note Springer Nature remains neutral with regard to jurisdictional claims in published maps and institutional affiliations.

Open Access This article is licensed under a Creative Commons Attribution 4.0 International License, which permits use, sharing, adaptation, distribution and reproduction in any medium or format, as long as you give appropriate credit to the original author(s) and the source, provide a link to the Creative Commons license, and indicate if changes were made. The images or other third party material in this article are included in the article's Creative Commons license, unless indicated otherwise in a credit line to the material. If material is not included in the article's Creative Commons license and your intended use is not permitted by statutory regulation or exceeds the permitted use, you will need to obtain permission directly from the copyright holder. To view a copy of this license, visit http://creativecommons.org/licenses/by/4.0/.

© The Author(s) 2021